

Tensor-based quantum phase difference estimation for large-scale demonstration

Shu Kanno,^{1,7*} Kenji Sugisaki,^{2,3,7} Hajime Nakamura,⁷ Hiroshi Yamauchi,^{4,7}
Rei Sakuma,^{5,7} Takao Kobayashi,¹ Qi Gao,^{1,7} Naoki Yamamoto^{6,7}

¹Mitsubishi Chemical Corporation, Science & Innovation Center, Yokohama, 227-8502, Japan

²Graduate School of Science and Technology, Keio University, 7-1 Shinkawasaki,
Saiwai-ku, Kawasaki, Kanagawa 212-0032, Japan

³Centre for Quantum Engineering, Research and Education, TCG Centres for Research
and Education in Science and Technology, Sector V, Salt Lake, Kolkata 700091, India

⁴SoftBank Corp., Research Institute of Advanced Technology, Tokyo, 105-7529, Japan

⁵Materials Informatics Initiative, RD Technology & Digital Transformation Center,
JSR Corporation, 3-103-9 Tonomachi, Kawasaki-ku, Kawasaki, 210-0821, Japan

⁶Department of Applied Physics and Physico-Informatics,

Keio University, 3-14-1 Hiyoshi, Kohoku-ku, Yokohama 223-8522, Japan

⁷Quantum Computing Center, Keio University, 3-14-1 Hiyoshi, Kohoku-ku,
Yokohama, 223-8522, Japan

*To whom correspondence should be addressed; E-mail: shu.kanno@quantum.keio.ac.jp

We develop an energy calculation algorithm leveraging quantum phase difference estimation (QPDE) scheme and a tensor-network-based unitary compression method in the preparation of superposition states and time-evolution gates. Alongside its efficient implementation, this algorithm reduces depolarization noise affections exponentially. We demonstrated energy gap calculations for one-dimensional Hubbard models on IBM superconducting devices using circuits up to 32-system (plus one-ancilla) qubits, a five-fold increase over previous QPE demonstrations, at the 7242 controlled-Z gate level of standard transpilation, keying a Q-CTRL error suppression module. Additionally, we propose a technique towards molecular executions using spatial orbital lo-

calization and index sorting, verified by an eight-qubit butadiene simulation. Since QPDE can handle the same objectives as QPE, our algorithm represents a leap forward in quantum computing on real devices.

Introduction

Abilities to calculate physical properties of materials with high accuracy are crucial for accelerating novel material discovery. The physical properties are mainly governed by the behavior of electrons in the material, while the number of possible electronic state configurations scales exponentially with system size. Approximation methods such as the Hartree–Fock (HF) method and density functional theory (DFT) are commonly used to cope with this exponential increase in classical computers. However, these methods often fail when electronic correlations are strong, leading to computational inaccuracies (1–3). Quantum computers are expected to overcome the accuracy limitations of classical computers because complex quantum states intractable by classical means can be efficiently represented using quantum superposition.

One of the most important quantum algorithms is quantum phase estimation (QPE) (4–12). QPE aims to find the eigenvalue corresponding to a given eigenstate of a system, representing the energy in quantum chemistry. In the conventional QPE (4), even if the approximate wave function $|\varphi\rangle$ is used, the full configuration interaction (FCI) energy can be obtained with probability proportional to the square of the overlap with the eigenfunction of the target Hamiltonian H . Thus, QPE can potentially compute FCI energies exponentially faster than classical methods, given appropriately prepared $|\varphi\rangle$.

We focus on Bayesian QPE (13), which utilizes Bayesian inference to narrow the confidence interval of the target phase value. The schematic is shown in Fig. 1(a); the probability of obtaining 0 in the measurement on the ancilla qubit constitutes a cosine curve for ε , the peak of which approximates the target phase. Controlled operations of time evolution gate U_{Trot} often require significant gate overhead in Bayesian (and conventional) QPE. For instance, a recent experiment for a two-qubit hydrogen molecule simulation on a trapped-ion device used 920 two-qubit gates (14). The overhead is particularly challenging in nearest-neighbor architectures like superconducting devices, which require qubit swaps for long-range operations. Hence, the quest for gate-efficient implementations is essential for large-scale QPE-type algorithms.

In this work, we propose a gate-efficient, QPE-type energy estimation algorithm. Our algorithm is based on the quantum phase difference estimation (QPDE) (15), a variant of QPE. QPDE can also compute FCI energy (16) but primarily targets the energy gap between states (e.g., ground and excited states). See Materials and Methods S1.1 for details. The important feature of QPDE is an avoidance of costly controlled- U_{Trot} operations. Instead, as shown in Fig. 1(b), it applies controlled operations to U_g and U_{ex} for preparing superpositions of ground and excited states. Our algorithm is a gate-efficient realization of QPDE; specifically, we classically prepare compressed versions of U_{Trot} as well as the controlled- U_g and U_{ex} as tensor networks, particularly matrix product operators (MPOs) (17–24). These classically prepared

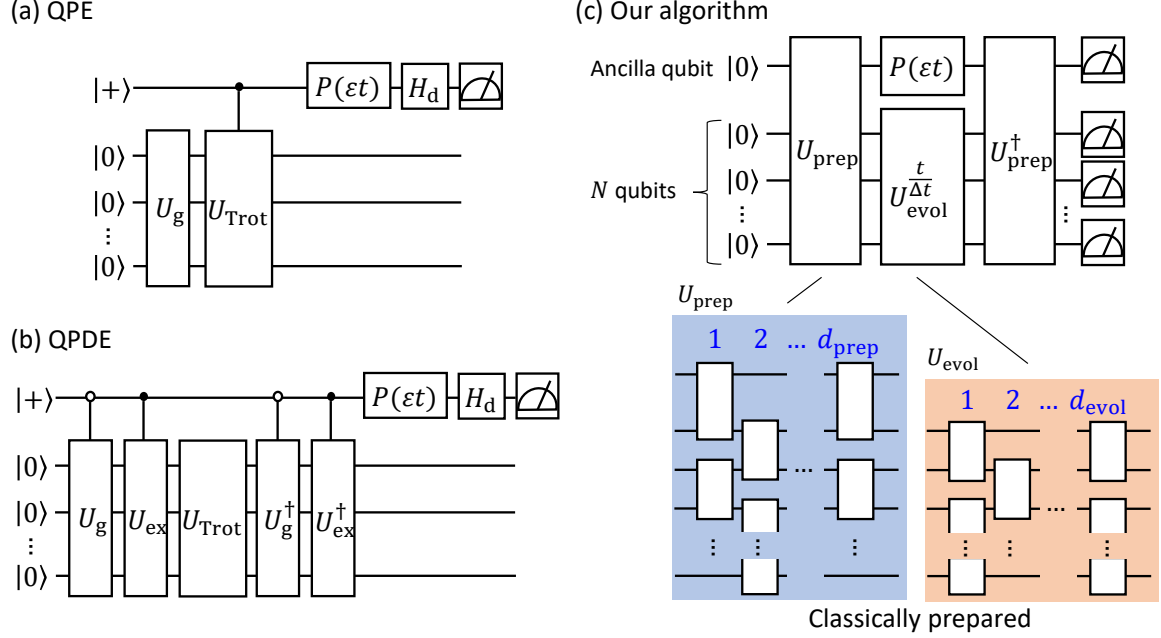


Fig. 1: Circuits for the Bayesian QPE-type algorithms and our algorithm. In all the figures, the topmost qubit is an ancilla qubit and the others are system qubits. $P(x)$ is a phase gate, and H_d is a Hadamard gate. U_g and U_{Trot} are the gate for approximate ground state preparation and the (controlled) time evolution, respectively. U_{prep} is an MPO for approximately preparing the superposition of ground and excited states, and U_{evol} is an MPO for approximating the time evolution operator. (a) Quantum phase estimation. (b) Quantum phase difference estimation. (c) Our algorithm.

operators are realized on a quantum circuit shown in Fig. 1(c). The proposed algorithm offers four main advantages. First, the resulting MPO-based circuits are constructed with nearest-neighbor gates in a brick-wall layout, facilitating parallelization without swaps. Second, the MPO can be efficiently prepared on classical computers and implemented on a quantum circuit, meaning that our algorithm does not suffer from a large amount of quantum-classical communication as in the variational quantum eigensolver (25). Third, because the initial superposition state is efficiently prepared as a matrix product state (MPS), the corresponding state preparation gate can be well approximated by an MPO. Finally, depolarizing noise effects are exponentially suppressed with respect to the number of qubits. The theoretical details can be seen in Materials and Methods S1.2 for the first three points and Supplementary Text S2.1 for the final point.

We apply our algorithm to calculate the energy gap for the one-dimensional Hubbard model, utilizing a quantum circuit with up to 32 qubits (plus one ancilla) on an IBM superconducting device, aided by a Q-CTRL error suppression module. Notably, this scale is five times larger than previous QPE studies (6). In addition, we investigate a 1,3-butadiene linear π conjugated molecule (hereafter referred to as butadiene). Butadiene's ground and excited state electronic

structures are of interest as the smallest π conjugated polyene, and it is also important in industry as a raw material for synthetic rubber (26). In the calculation of butadiene, a one-dimensional Hamiltonian was constructed by using newly developed orbital localization and index reordering techniques. Finally, recall that the MPO-based time-evolution gate of small time Δt can be classically implemented, while its concatenation for long-time simulation cannot. Thus, the quantum advantage of this algorithm lies in the time evolution circuit.

Tensor-based phase difference estimation algorithm

The entire estimation algorithm is summarized to Algorithm 1 given in Materials and Methods S1.1, and here we describe the procedure sketch. For each iteration, the multiple circuits with different parameters ε determined from the prior distribution are executed, where the prior and posterior distributions are assumed to be Gaussian, and the total time t is determined from the variance of the prior distribution. In advance to executing the quantum algorithm with the circuit Fig. 1(c), we compute MPOs corresponding to U_{prep} and U_{evol} by classical means, followed by preparing their gate realization.

The quantum algorithm is executed as follows; we prepare the superposition state using U_{prep} gate, evolve the state by operating U_{evol} by $t/\Delta t$ times, operate the phase gate with εt , uncompute the state using U_{prep}^\dagger gate, and measure all qubits to obtain the probability of getting all 0. The number of depths of U_{prep} and U_{evol} are d_{prep} and d_{evol} , respectively. We repeat this procedure with different ε to obtain the likelihood function which can be further approximated by Gaussian distribution. The posterior distribution is calculated to update the confidence interval of ε , and the posterior distribution is used as the prior distribution for the next iteration.

We can also calculate the FCI energy by simplifying the procedure. That is, the value of gap with a negative sign corresponds to the FCI energy when $|\psi_{\text{ex}}\rangle$ is a vacuum state (16), and see Supplementary Text S2.2 for the demonstration of the FCI energy calculation. Note that by extending the tensor structure from an MPO to a complicated tensor such as a tree tensor, our algorithm would be useful even for all-to-all connected devices such as trapped-ion and neutral atom devices since the long-distance transport of ions (or atoms) is costly in practice (27).

Benchmark on the unitary compression method

We provide a brief comparison of the proposed unitary compression method with conventional methods for state preparation and time evolution circuits. We consider the following one-dimensional Hubbard model:

$$H = -T \sum_{q=1}^{n_s-1} \sum_{\sigma \in \{\uparrow, \downarrow\}} (a_{q+1\sigma}^\dagger a_{q\sigma} + a_{q\sigma}^\dagger a_{q+1\sigma}) + U \sum_{q=1}^{n_s} n_{q\uparrow} n_{q\downarrow} - \frac{U}{2} \sum_{q=1}^{n_s} (n_{q\uparrow} + n_{q\downarrow}), \quad (1)$$

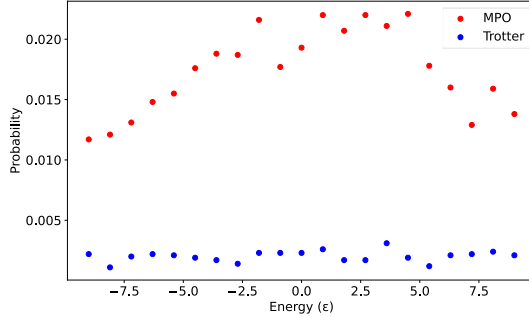


Fig. 2: Comparison of the time evolution circuits (nine qubits) using the Eagle device *ibm_osaka*.

where q (σ) is the orbital (spin) index, $T = 1$ is the hopping energy so that energy is unitless, U is the on-site Coulomb energy, $a_{q\sigma}^\dagger$ ($a_{q\sigma}$) is the creation (annihilation) operator, and $n_{q\sigma}$ is the number operator $n_{q\sigma} = a_{q\sigma}^\dagger a_{q\sigma}$. In this study, we choose $U = 10$, which corresponds to the strong correlation regime, and we consider $n_s = 4$, i.e., eight-system qubit model in this section, and the fermion-qubit mapping is a Jordan–Wigner transformation with an up-down qubit sequence $1 \uparrow, 1 \downarrow, 2 \uparrow, \dots, n_s \downarrow$.

The metric to evaluate the U_{prep} approximation for the state preparation circuit is $f(U_{\text{prep}}; |\text{MPS}\rangle)$ represented by

$$f(U_{\text{prep}}; |\text{MPS}\rangle) = \langle \text{MPS} | U_{\text{prep}} | 0 \rangle^{\otimes N+1}, \quad (2)$$

where N is the number of system qubits and $N = 2n_s$ in the Hubbard model. Because we consider only the real wave function in this study, the metric is real. $|\text{MPS}\rangle$ is an MPS calculated for the ground and first-excited states using the density matrix renormalization group (DMRG) (28, 29). Because we confirmed that the DMRG result was almost the same as the exact solution in the current eight-qubit model, $f(U_{\text{prep}}; |\text{MPS}\rangle)$ is close to the square root of fidelity $f(U_{\text{prep}}; |\psi_{\text{target}}\rangle)$, where $|\psi_{\text{target}}\rangle = \frac{1}{\sqrt{2}}(|0\rangle|\psi_g\rangle + |1\rangle|\psi_{\text{ex}}\rangle)$, and $|\psi_g\rangle$ and $|\psi_{\text{ex}}\rangle$ are approximate ground and excited states obtained using the DMRG, respectively. The metric $f(U_{\text{prep}}; |\text{MPS}\rangle)$ takes the maximum value 1 when $U_{\text{prep}} |0\rangle^{\otimes N+1} = |\text{MPS}\rangle$. The coefficient of the Hartree–Fock configuration in the exact ground state is 0.66. On the other hand, the $f(U_{\text{prep}}; |\text{MPS}\rangle)$ for this model was 0.99 at $d_{\text{prep}} = 6$, which indicates that the U_{prep} can prepare states with high accuracy.

The error metric of the U_{evol} approximation in the time evolution circuit is $\delta(U_{\text{evol}}; U_{\text{ref}})$ as in (22):

$$\delta(U_{\text{evol}}; U_{\text{ref}}) = \sqrt{2 - \text{Re} \text{Tr} \left[U_{\text{ref}}^\dagger U_{\text{evol}} \right]^{\frac{1}{N}}}, \quad (3)$$

where U_{ref} is a reference MPO prepared by converting the time evolution operator to an MPO (see Materials and Methods S1.2 for details). $\frac{1}{N}$ is the normalization factor. From the related reason in the state preparation of $|\text{MPS}\rangle \approx |\psi_{\text{target}}\rangle$, $\delta(U_{\text{evol}}; U_{\text{ref}})$ is close to $\delta(U_{\text{evol}}; e^{-iH\Delta t})$ in

the current model. We choose $\Delta t = 0.1$ throughout this study. $\delta(U_{\text{evol}}; U_{\text{ref}})$ takes the minimum value 0 when $U_{\text{evol}} = U_{\text{ref}}$. $\delta(U_{\text{evol}}; U_{\text{ref}})$ at $d_{\text{evol}} = 5$ was 4.3×10^{-3} , and $\delta(U_{\text{evol}}; e^{-iH\Delta t})$ of the first- and second-order Trotter approximations were 2.2×10^{-2} and 1.6×10^{-3} , respectively. The values suggest that the accuracy of prepared U_{evol} is between first- and second-order Trotter approximations, which corresponds to the tendency in the previous study (22).

To confirm the circuit execution efficiency, we compared the results of the measured probability distributions in the circuit of Fig. 1(c) run on a real device with U_{evol} as is and replaced by the first-order Trotter approximation. The variance of the prior distribution is 9.0 which corresponds to $t = 0.2$ (see Materials and Methods S1.1), the device is Eagle *ibm_osaka*, $d_{\text{prep}} = 6$, and the error suppression module appeared in the subsequent sections is not used here. The number of shots is 10,000 in the real device execution of this study. The number of two-qubit gates in the circuit after transpilation in Qiskit (30) was 216 for U_{prep} and 234 for the first-order Trotter approximation. The results are shown in Fig. 2. The plots by U_{evol} (red) show peaks, while the Trotter results (blue) show a uniform distribution. These results indicate that the unitary compression has a high execution efficiency for real devices.

Demonstration of the algorithm

We show the demonstration for the Hubbard model in Eq. (1). Figure 3(a) shows the result of a noiseless simulator for our algorithm with $n_s = 4$, i.e., a nine-qubit circuit including one ancilla qubit, where $d_{\text{prep}} = 6$ and $d_{\text{evol}} = 5$ which are the same setting in the previous section. As the iteration increases, the mean value of the posterior distribution (circle) approaches the exact energy (dashed line), and the standard deviation (error bar) becomes smaller. The mean value of the posterior distribution in the final iteration is 0.224 ± 0.005 , and the exact value is 0.254; i.e., the bias error 0.030 remains. From the results of $\delta(U_{\text{evol}}; U_{\text{ref}})$ in the previous section, the accuracy is improved by increasing d_{evol} from five; in fact, if $d_{\text{evol}} = 8$ and 10, the bias error decreases to 0.020 and 0.012, respectively. The probabilities taken from each circuit with ε (energy parameter) determined from the prior distribution are shown in red, and a peak at the mean value can be seen.

Figure 3(b,c,d) show the results on the real device *ibm_torino*, where we used an error suppression module FireOpal in Q-CTRL (31–33). Certainly in Fig. 3(b), the maximum probability of 0.75 at the first iteration was reduced to 0.0035 at the sixth iteration due to noise. Nevertheless, it was observed that the mean values move toward the exact solution, and the variance also decreases as the iterations increase. That is, our algorithm worked in the nine-qubit circuit, where the final value was 0.294 ± 0.359 . The two-qubit gate counts in the circuit in the final iteration is 2984/2274, where hereafter we regard the gate count value before and after slash as the value before and after the error suppression, respectively. Note that the error suppression was executed after the Qiskit transpilation.

Figures 3(c) and (d) are results for $n_s = 10$ and 16 by using 21 and 33 qubit circuits, where $f(U_{\text{prep}}; |\text{MPS}\rangle)$ in $d_{\text{evol}} = 12$ are 0.92 and 0.81, respectively. d_{prep} was fixed to five since

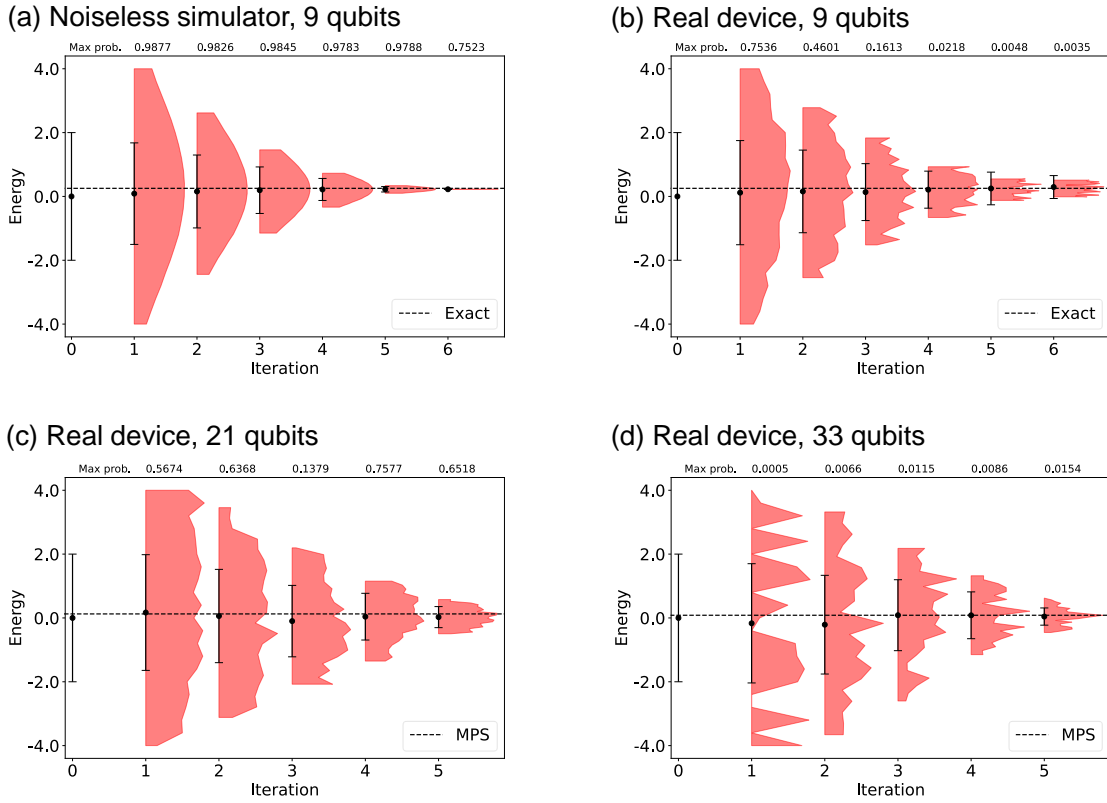


Fig. 3: Demonstration of our algorithm in the one-dimensional Hubbard models using (a) the noiseless simulator and (b,c,d) the Heron device *ibm_torino* with the error suppression. The circle and error bar denote the mean value and standard deviation, respectively, of the posterior distribution in each iteration. The sampled probabilities are shown in red, and each plot is normalized by the maximum value in each iteration, which is shown at the top of the plot.

the values $\delta(U_{\text{evol}}; U_{\text{ref}})$ tend not to depend on the model size, where the values are 4.6×10^{-3} in 20 system qubits, 4.5×10^{-3} in 32 qubits, and 5.3×10^{-3} even in 100 qubits. Although there are some numerical instabilities, such as in the low probability in the first iteration in the figure 3(d), we still obtain final gap values of 0.026 ± 0.330 and 0.043 ± 0.270 for 21 and 33 qubit circuits, and the MPS gap values for references are 0.125 and 0.084, respectively. As in Supplementary Text S2.1, we theoretically confirm that our algorithm does not change the peak top value if a depolarization noise is assumed, which is the same as in the previous Bayesian QPE algorithms (13, 16). Furthermore, the effect of depolarization noise in a circuit execution exponentially reduces for N (with a fixed error rate). In fact, while a distribution for a nine-qubit model becomes blurred due to noise on the final iteration, sharp peaks can be found for 21- and 33-qubit models. Additionally, the number of two-qubit gates in the final iteration of the 33-qubit circuit is 7242/794, nearly 10 times gate reduction by the error suppression was found. As a result, our algorithm can be performed on more than five times larger systems in terms of the number of qubits than the previous QPE study of six qubit systems (6). Note that for the signal weakening in the first iteration on the 33 qubit demonstration, it is difficult for us to fully identify the cause due to the multiple error suppression components in FireOpal (see also Materials and Methods S1.1), but it may be relevant that the number of gates in the circuit after the error suppression was slightly high, where the gate counts in the first and final iterations were 819 and 794, respectively. We also note that there were only a few signals when the suppression module was not enabled, and the probabilities were too low to obtain meaningful results on the 21-qubit circuit (see Supplementary Text S2.1).

We next show the result of our algorithm to a realistic chemical model. The target molecule is butadiene, and the Hamiltonian is an eight-qubit complete active space configuration interaction (CASCI) (4e 4o) problem consisting of π and π^* orbitals (see Materials and Methods S1.3). The obstacle to applying our algorithm in this model is that the molecular orbitals are delocalized throughout the molecule and thus the Hamiltonian is not one-dimensional. Therefore, we propose a general procedure to convert such Hamiltonian to a one-dimensional one, as shown in Fig. 4(a). We first localized the orbitals by Boys localization (35). Then, the orbital indices are reordered by exchange interaction. Specifically, we introduce the cost function referencing the proposal in the context of tensor networks in classical calculations (36),

$$C = \sum_{ij} K_{ij} D_{ij}^2, \quad (4)$$

where i and j are orbital indices, K_{ij} is the value of the exchange interaction between orbitals, and D_{ij} is the distance between orbitals when the orbital indices are arranged in a one-dimensional list. We show an example of C in Fig. 4(b). C was optimized with a genetic algorithm (see Materials and Methods S1.3), and its initial and final value is 0.0506 to 0.0097, respectively. Finally, the reordered model was mapped to qubits by Jordan–Wigner transformation with the up-down qubit sequence.

We calculate the energy gap between the lowest spin-singlet and triplet states. The values of

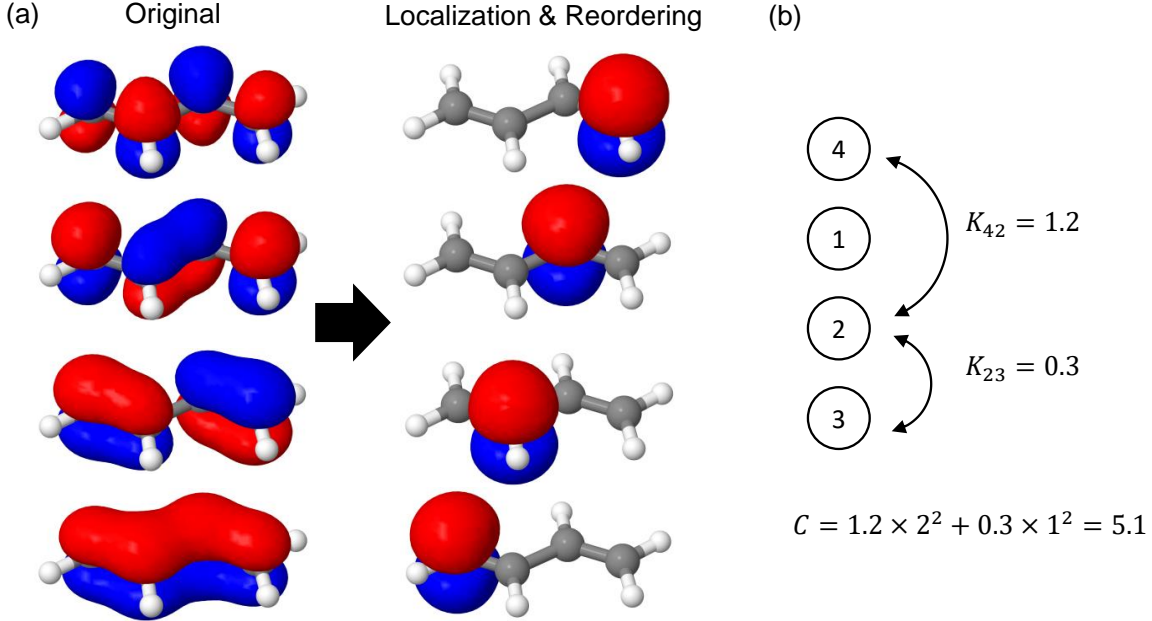
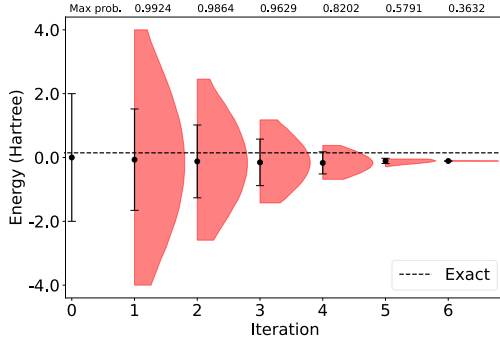


Fig. 4: Procedure for converting the molecular Hamiltonian to a one-dimensional one. (a) Orbitals before and after the procedure. The structures are drawn by Jmol (34). (b) Example of the cost function.

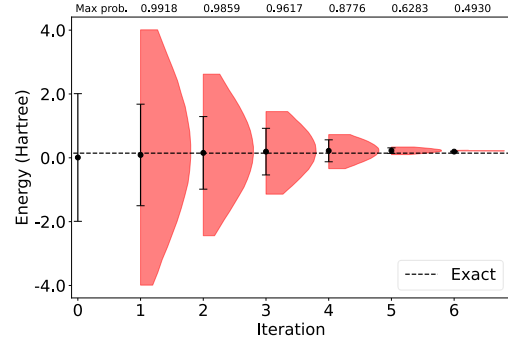
the metric $f(U_{\text{prep}}; |\text{MPS}\rangle)$ in the original and in the one-dimensionalized models in $d_{\text{prep}} = 8$ were 0.98 and 0.99, which indicates that U_{prep} is producing high fidelity despite the fact that both the ground and excited state cannot be approximated by a single configuration due to orbital localization. The values of $\delta(U_{\text{evol}}; U_{\text{ref}})$ in $d_{\text{evol}} = 10$ were 1.3×10^{-2} and 7.5×10^{-3} , respectively, more than 40% reduction in U_{evol} . Note that although the value of the improvement in the metric itself is not large, the improvement is significant because U_{evol} is applied $t/\Delta t$ times.

Figure 5 shows the results of our algorithm for each model. The gap values in the original and one-dimensional models for the noiseless simulator in Figs. 5(a) and (b) are 0.194 ± 0.013 and -0.111 ± 0.005 , and the values for the real device in Figs. 5(c) and (d) are 0.296 ± 0.518 and 0.235 ± 0.619 , and the gate counts are 3645/1871 and 4485/1300, respectively. The exact gap is 0.146 in this system. The results suggest that the one-dimensional processing can extend the range of applications of our algorithm. In the real device results of Figs. 5(c) and (d), the trend is blurred on the real device, and the change of confidence intervals is slow after the fourth iteration. As described in the Hubbard model results, this is a property in a small-scale execution and thus will not be an issue in a large system.

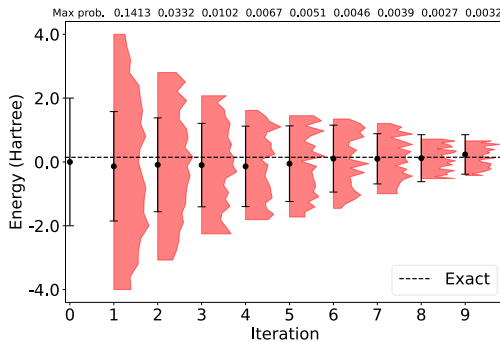
(a) Noiseless simulator, Molecular orbitals



(b) Noiseless simulator, Localized orbitals



(c) Real device, Molecular orbitals



(d) Real device, Localized orbitals

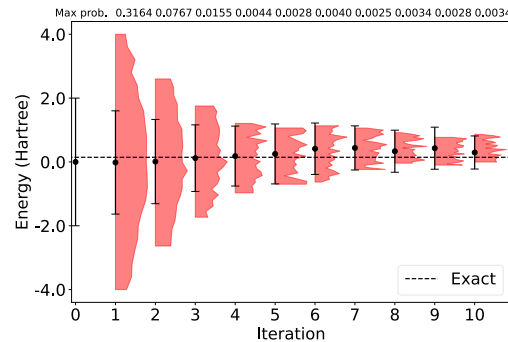


Fig. 5: Demonstration of our algorithm in butadiene (nine-qubit circuit) using (a,b) the noiseless simulator and (c,d) the Heron device *ibm_torino* with the error suppression. The circle and error bar denote the mean value and standard deviation, respectively, of the posterior distribution in the iteration. The sampled probabilities are shown in red, and each plot is normalized by the maximum value in each iteration, which is shown at the top of the plot.

Outlook

We have proposed a gate-efficient and noise-robust quantum phase estimation-type algorithm based on unitary compression by tensor networks. We applied the algorithm to a one-dimensional Hubbard model and confirmed its effectiveness on a real superconducting device, utilizing an error suppression module, with circuits up to 33 qubits including one ancilla qubit. Furthermore, for the calculation of chemical models, we proposed a procedure to convert the model composed of molecular orbitals into a one-dimensional model by orbital localization and re-ordering, achieving over 40% improvement in the error metric. These results enable large-scale implementations of quantum phase estimation-type algorithms.

The most significant challenge is an improvement of estimation to achieve chemical accuracy. A deeper MPO improves accuracy, but in general, the computational cost increases exponentially with depth. Since our unitary compression can be extended to tensor networks other than MPO, tensor networks that account for non-linearity in device connectivity — for example heavy hex on IBM devices (37) or two-dimensional grids on Google devices (38). In the case of ion- or atom-trapped hardware, physical constraints on the transport of the particles would influence the optimal tensor structure for the algorithm. Alternatively, integrating quantum-classical hybrid-optimized circuit to U_{prep} can improve accuracy (20, 25, 39).

Finally, in addition to QPE forming the basis of quantum computation, the technique we proposed for superposition state preparation to avoid long-range interactions involving an ancilla qubit can be used for more general circuit compilation (40). Hence, the proposed algorithms or techniques have potential applications in other fields besides chemistry, such as the Harrow–Hassidim–Lloyd algorithm (41) in machine learning.

Acknowledgements

This work was supported by Quantum Leap Flagship Program (Grant No. JPMXS0118067285 and No. JPMXS0120319794) from the MEXT, Japan. A part of this work was performed for Council for Science, Technology and Innovation (CSTI), Cross-ministerial Strategic Innovation Promotion Program (SIP), “Promoting the application of advanced quantum technology platforms to social issues”(Funding agency: QST). The part of calculations was performed on the Mitsubishi Chemical Corporation (MCC) high-performance computer (HPC) system “NAYUTA”, where “NAYUTA” is a nickname for MCC HPC and is not a product or service name of MCC. We acknowledge the use of IBM Quantum services for experiments in this paper. The views expressed are those of the authors, and do not reflect the official policy or position of IBM or the IBM Quantum team. This work is partly supported by Q-CTRL. S.K. thanks to Yuki Sato, Toshinari Itoko, Hiroyoshi Kurogi, Hiroshi Watanabe, Yoshiharu Mori, Takashi Abe, Miho Hatanaka, and Kaito Wada for fruitful discussions, Hajime Sugiyama for the technical support on HPC, Kimberlee Keithley for assistance in reviewing the English manuscript. K.S. acknowledges support from Center of Innovations for Sustainable Quantum AI (JPMJPF2221)

from JST, Japan, and Grants-in-Aid for Scientific Research C (21K03407) and for Transformative Research Area B (23H03819).

References and Notes

1. B. Bauer, S. Bravyi, M. Motta, G. Kin-Lic Chan, *Chem. Rev.* **120**, 12685 (2020).
2. Y. Cao, *et al.*, *Chem. Rev.* **119**, 10856 (2019).
3. A. J. Cohen, P. Mori-Sánchez, W. Yang, *Chem Rev* **112**, 289 (2012).
4. M. A. Nielsen, I. L. Chuang, *Quantum Computation and Quantum Information: 10th Anniversary Edition* (Cambridge University Press, 2010).
5. A. Yu. Kitaev, *arXiv.9511026 [quant-ph]* (1995).
6. N. S. Blunt, L. Caune, R. Izsák, E. T. Campbell, N. Holzmann, *PRX Quantum* **4**, 040341 (2023).
7. S. Paesani, *et al.*, *Phys. Rev. Lett.* **118**, 100503 (2017).
8. P. J. J. O’Malley, *et al.*, *Phys. Rev. X* **6**, 031007 (2016).
9. B. P. Lanyon, *et al.*, *Nat. Chem.* **2**, 106 (2010).
10. J. Du, *et al.*, *Phys. Rev. Lett.* **104**, 030502 (2010).
11. Y. Wang, *et al.*, *ACS Nano* **9**, 7769 (2015).
12. R. Santagati, *et al.*, *Sci Adv* **4**, eaap9646 (2018).
13. N. Wiebe, C. Granade, *Phys. Rev. Lett.* **117**, 010503 (2016).
14. K. Yamamoto, S. Duffield, Y. Kikuchi, D. Muñoz Ramo, *Phys. Rev. Res.* **6**, 013221 (2024).
15. K. Sugisaki, *et al.*, *Phys. Chem. Chem. Phys.* **23**, 20152 (2021).
16. K. Sugisaki, *et al.*, *J. Phys. Chem. Lett.* **12**, 11085 (2021).
17. B. Anselme Martin, T. Ayral, F. Jamet, M. J. Rančić, P. Simon, *Phys. Rev. A* **109**, 062437 (2024).
18. M. S. Rudolph, J. Chen, J. Miller, A. Acharya, A. Perdomo-Ortiz, *arXiv.2209.00595 [quant-ph]* (2022).
19. S.-J. Ran, *Phys. Rev. A* **101**, 032310 (2020).

20. J. Dborin, F. Barratt, V. Wimalaweera, L. Wright, A. G. Green, *Quantum Sci. Technol.* **7**, 035014 (2022).
21. J. Dborin, *et al.*, *Nat. Commun.* **13**, 5977 (2022).
22. L. Causer, F. Jung, A. Mitra, F. Pollmann, A. Gammon-Smith, *Phys. Rev. Res.* **6** (2024).
23. S.-H. Lin, R. Dilip, A. G. Green, A. Smith, F. Pollmann, *PRX Quantum* **2**, 010342 (2021).
24. T. Shirakawa, H. Ueda, S. Yunoki, *arXiv.2112.14524 [quant-ph]* (2021).
25. A. Peruzzo, *et al.*, *Nat. Commun.* **5**, 4213 (2014).
26. J. Yang, P. Wang, H. Neumann, R. Jackstell, M. Beller, *Ind. Chem. Mater.* **1**, 155 (2023).
27. K. R. Brown, J. Kim, C. Monroe, *npj Quantum Information* **2**, 1 (2016).
28. S. R. White, *Phys. Rev. Lett.* **69**, 2863 (1992).
29. U. Schollwöck, *Ann. Phys.* **326**, 96 (2011).
30. A. Javadi-Abhari, *et al.*, *arXiv.2405.08810 [quant-ph]* (2024).
31. P. S. Mundada, *et al.*, *Phys. Rev. Appl.* **20**, 024034 (2023).
32. N. Sachdeva, *et al.*, *arXiv.2406.01743 [quant-ph]* (2024).
33. Y. Baum, *et al.*, *PRX Quantum* **2**, 040324 (2021).
34. Jmol development team, Jmol (2016).
35. J. M. Foster, S. F. Boys, *Rev. Mod. Phys.* **32**, 300 (1960).
36. N. Nakatani, G. K.-L. Chan, *J. Chem. Phys.* **138**, 134113 (2013).
37. Y. Kim, *et al.*, *Nature* **618**, 500 (2023).
38. F. Arute, *et al.*, *Nature* **574**, 505 (2019).
39. K. Nakaji, *et al.*, *arXiv.2401.09253 [quant-ph]* (2024).
40. S. Kanno, *et al.*, *npj Quantum Information* **10**, 1 (2024).
41. A. W. Harrow, A. Hassidim, S. Lloyd, *Phys. Rev. Lett.* **103**, 150502 (2009).
42. K. Sugisaki, *et al.*, *ACS Cent Sci* **5**, 167 (2019).
43. F. Vatan, C. Williams, *Phys. Rev. A* **69**, 032315 (2004).

44. B. Drury, P. Love, *J. Phys. A: Math. Theor.* **41**, 395305 (2008).
45. M. Fishman, S. R. White, E. Miles Stoudenmire, *arXiv.2007.14822 [cs.MS]* (2020).
46. C. R. Harris, *et al.*, *Nature* **585**, 357 (2020).
47. Q. Sun, *et al.*, *J. Chem. Phys.* **153**, 024109 (2020).
48. L.-P. Wang, C. Song, *J. Chem. Phys.* **144**, 214108 (2016).
49. F.-A. Fortin, F. Rainville, M.-A. Gardner, M. Parizeau, C. Gagné, *J. Mach. Learn. Res.* **13**, 2171 (2012).
50. J. Tilly, *et al.*, *Phys. Rep.* **986**, 1 (2022).
51. A. Miller, Z. Zimborás, S. Knecht, S. Maniscalco, G. García-Pérez, *PRX quantum* **4** (2023).

Supplementary Materials

S1 Materials and Methods

S1.1 Procedure of the algorithm

Algorithm 1 shows the procedure of our algorithm. In each iteration, we update the distribution along with the measurement results. For ε , t , and \vec{x} (i.e., the computational-basis measurement result represented by a binary sequence), there is a relation among prior distribution $P(\varepsilon)$, likelihood function $P(\vec{x}|\varepsilon)$, and posterior distribution $P(\varepsilon|\vec{x})$ called the Bayes theorem,

$$P(\varepsilon|\vec{x}) \propto P(\vec{x}|\varepsilon)P(\varepsilon). \quad (\text{S1.1})$$

The calculated posterior distribution is used as the prior distribution in the next iteration. In this work, we take the Bayes setting with Gaussian probability distribution $P(z) = \mathcal{N}(z; \mu, \sigma^2)$ of the random variable z , with mean μ and variance σ^2 . We specifically choose the Gaussian prior $P(\varepsilon) = \mathcal{N}(\varepsilon; \mu_{\text{prior}}, \sigma_{\text{prior}}^2)$.

This study considers distributions over two patterns for all qubits $\vec{x} \in \{\vec{0}, \text{others}\}$ where $\vec{0}$ represents all zero measurements, which corresponds to the two measurement patterns for an ancilla qubit, $\{0, 1\}$, in the previous studies (13, 42). Then, as shown just later, the likelihood function with respect to ε can be well approximated by the Gaussian $P(\vec{0}|\varepsilon) = \mathcal{N}(\varepsilon; \mu_{\text{lh}}, \sigma_{\text{lh}}^2)$. As a result, the posterior distribution keeps the form of Gaussian as $P(\varepsilon|\vec{0}) = \mathcal{N}(\varepsilon; \mu_{\text{post}}, \sigma_{\text{post}}^2)$, where

$$\mu_{\text{post}} = \frac{\sigma_{\text{prior}}^2 \mu_{\text{lh}} + \sigma_{\text{lh}}^2 \mu_{\text{prior}}}{\sigma_{\text{lh}}^2 + \sigma_{\text{prior}}^2}, \quad (\text{S1.2})$$

$$\sigma_{\text{post}}^2 = \frac{\sigma_{\text{prior}}^2 \sigma_{\text{lh}}^2}{\sigma_{\text{lh}}^2 + \sigma_{\text{prior}}^2}. \quad (\text{S1.3})$$

In the circuit implementation in Fig. 1(c), we assume

$$U_{\text{prep}} |0\rangle^{\otimes N+1} \approx \frac{1}{\sqrt{2}}(|0\rangle |\psi_{\text{g}}\rangle + |1\rangle |\psi_{\text{ex}}\rangle), \quad (\text{S1.4})$$

$$U_{\text{evol}} \approx e^{-iH\Delta t}, \quad (\text{S1.5})$$

where $|\psi_{\text{g}}\rangle$ and $|\psi_{\text{ex}}\rangle$ are the ground and excited states, respectively, and N is the number of system qubits. The wave function after operating U_{evol} and $P(\varepsilon t)$ is

$$\begin{aligned} & (P(\varepsilon t) \otimes U_{\text{evol}}) \frac{1}{\sqrt{2}}(|0\rangle |\psi_{\text{g}}\rangle + |1\rangle |\psi_{\text{ex}}\rangle) \\ & \approx \frac{1}{\sqrt{2}}(e^{-iE_{\text{g}}t} |0\rangle |\psi_{\text{g}}\rangle + e^{-i(E_{\text{ex}}-\varepsilon)t} |1\rangle |\psi_{\text{ex}}\rangle), \end{aligned} \quad (\text{S1.6})$$

Algorithm 1: Tensor-based quantum phase difference estimation

Input: Initial mean (variance) as a prior Gaussian distribution μ_{init} (σ_{init}^2), the number of sample points m , the number of shots R , single time step Δt

// Initial preparation

1 $\mu_{\text{prior}} \leftarrow \mu_{\text{init}}$
2 $\sigma_{\text{prior}}^2 \leftarrow \sigma_{\text{init}}^2$
3 $iter \leftarrow 1$

// Estimation loop

4 **while** true **do**

5 $t \leftarrow 1.8/\sigma_{\text{prior}}^2$
6 $\vec{\varepsilon}_{\text{list}} \leftarrow$ make a list by selecting m points equally in the interval from $\mu_{\text{prior}} - \sigma_{\text{prior}}^2$ to $\mu_{\text{prior}} + \sigma_{\text{prior}}^2$
7 $\vec{p}_{\text{list}} \leftarrow$ empty list
8 **for** ε in $\vec{\varepsilon}_{\text{list}}$ **do**
9 Execute the circuit in Fig. 1(c) with t , Δt , ε , and shot number R
10 Obtain the probability p that 0 is measured in all qubits of the circuit
11 Append the value pair (ε, p) to \vec{p}_{list}

// Mean and variance of likelihood function

12 $\mu_{\text{lh}}, \sigma_{\text{lh}}^2 \leftarrow$ calculate from the Gaussian fitting of \vec{p}_{list}

// Mean and variance of posterior distribution

13 Calculate $\mu_{\text{post}}, \sigma_{\text{post}}^2$ by Eqs. (S1.2) and (S1.3) using $\mu_{\text{prior}}, \sigma_{\text{prior}}^2, \mu_{\text{lh}}$, and σ_{lh}^2

14 Print $iter, \vec{p}_{\text{list}}, \mu_{\text{post}}$, and σ_{post}^2

15 **if** a termination condition, such as threshold of σ_{post}^2 , is satisfied **then**

16 **break**

17 **else**

18 $\mu_{\text{prior}} \leftarrow \mu_{\text{post}}$
19 $\sigma_{\text{prior}}^2 \leftarrow \sigma_{\text{post}}^2$
20 $iter \leftarrow iter + 1$

where E_g and E_{ex} are the eigenvalues of the ground and excited states, respectively. Suppose here the state before the measurement as

$$|\phi\rangle = \frac{1}{\sqrt{2}} U_{\text{prep}}^\dagger (e^{-iE_g t} |0\rangle |\psi_g\rangle + e^{-i(E_{\text{ex}} - \varepsilon)t} |1\rangle |\psi_{\text{ex}}\rangle). \quad (\text{S1.7})$$

Then, the probability of having the measurement result $\vec{x} = \vec{0}$, i.e., the likelihood function $P(\vec{0}|\varepsilon)$, is given by

$$\begin{aligned} P(\vec{0}|\varepsilon) &= \text{Tr} \left[|0\rangle \langle 0|^{\otimes N+1} |\phi\rangle \langle \phi| \right] \\ &\approx \frac{1}{4} |(\langle 0| \langle \psi_g | + \langle 1| \langle \psi_{\text{ex}} |)(e^{-iE_g t} |0\rangle |\psi_g\rangle + e^{-i(E_{\text{ex}} - \varepsilon)t} |1\rangle |\psi_{\text{ex}}\rangle)|^2 \\ &= \frac{1}{4} |e^{-iE_g t} + e^{-i(E_{\text{ex}} - \varepsilon)t}|^2 \\ &= \frac{1}{2} (1 + \cos(E_{\text{gap}} - \varepsilon)t), \end{aligned} \quad (\text{S1.8})$$

and the final expression can be approximated as

$$P(\vec{0}|\varepsilon) \approx \exp \left\{ -\frac{t^2}{4} (\varepsilon - E_{\text{gap}})^2 \right\}, \quad (\text{S1.9})$$

where E_{gap} is a energy gap represented as $E_{\text{gap}} = E_{\text{ex}} - E_g$. Therefore, by calculating the probability that all qubits are measured at 0 in an appropriate range of ε , the likelihood function can be approximated by a Gaussian distribution.

The number of two-qubit gates required to execute the circuit of Fig. 1(c) is at most

$$3 \times \left\{ N \times \lceil \frac{d_{\text{prep}}}{2} \rceil \times 2 + (N-1) \times \lceil \frac{d_{\text{evol}}}{2} \rceil \times \frac{t}{\Delta t} \right\}, \quad (\text{S1.10})$$

where the first 3 comes from the fact that any two-qubit gate can be executed with up to 3 native two-qubit gates (43, 44). In the real device execution, the gate count would be smaller than the above value due to the transpilation and the error suppression, where optimization level 3 was adopted in the Qiskit transpilation.

Our phase difference estimation algorithm is implemented in Qiskit (30) with the FireOpal error suppression module (31, 32) of the Python language. FireOpal is a package of deterministic error-suppression workflow composed of a depth reduction and logical transpilation, an error-aware hardware mapping, an elimination of circuit crosstalk (dynamical decoupling), an optimized gate replacement (including AI-powered analog-level gate optimization), an measurement-error mitigation (including AI-driven calibration routine) (31). We choose $m = 21$, $R = 10,000$, and $\Delta t = 0.1$. σ_{init}^2 is 9.0 in the result of Fig. 2 and is 4.0 in the other results. $\mu_{\text{init}} = 0.0$ in most of the cases, but when the peak of the likelihood function diverged in the noiseless simulation, it deviated by 0.01. The total time t is chosen as $1.8/\sigma_{\text{prior}}^2$. For the

noiseless simulation, the termination condition of our algorithm is achieving $\sigma_{\text{post}}^2 \leq 0.005$. In the real device execution, the algorithm stopped around 4,000-8,000 two-qubit gates in a circuit before the suppression due to FireOpal (or IBM Quantum Platform) system errors, e.g., QASM upload size limit, before reaching the above conditions. The prior Gaussian distribution is used as the initial guess of the Gaussian fitting of the likelihood function.

S1.2 Unitary compression

The unitary compression of U_{evol} is based on the procedure in Ref. (22). We approximate the time evolution in a single step, where the error in the simulation for a total time t is bounded by $\|e^{-iHt} - U_{\text{evol}}^{\frac{t}{\Delta t}}\| \leq \frac{t}{\Delta t} \|e^{-iH\Delta t} - U_{\text{evol}}\|$, where $\|\cdot\|$ is the operator norm. We first prepare an MPO U_{ref}^\dagger corresponding to $e^{iH\Delta t}$ by using the second-order Trotter approximation for 100 sliced time steps, $\Delta t/100$. Specifically, we start from an identity MPO and multiply by the time evolution MPO of the sliced step for each term of H , which is expanded by the tensor product of Pauli matrices. To prevent divergence of the bond dimension, a sweep of singular value decomposition (SVD) truncating singular values below a threshold value of 10^{-12} was performed for the MPO each time applying the time evolution of the term. Next, we optimize a brick-wall MPO U_{evol} to approximate U_{ref} . We consider minimizing the squared Frobenius norm of these operators,

$$\begin{aligned} \|U_{\text{ref}} - U_{\text{evol}}\|_F^2 &= \text{Tr}\left[U_{\text{ref}}^\dagger U_{\text{ref}}\right] + \text{Tr}\left[U_{\text{evol}}^\dagger U_{\text{evol}}\right] - 2 \text{Re} \text{Tr}\left[U_{\text{ref}}^\dagger U_{\text{evol}}\right] \\ &= 2^{N+1} - 2 \text{Re} \text{Tr}\left[U_{\text{ref}}^\dagger U_{\text{evol}}\right]. \end{aligned} \quad (\text{S1.11})$$

The norm can be minimized by maximizing the $\text{Re} \text{Tr}\left[U_{\text{ref}}^\dagger U_{\text{evol}}\right]$ of the last term.

Figure S1.1 shows the optimization procedure. The orange tensor network represent U_{ref}^\dagger , and the blue brick-wall tensor network represent U_{evol} in Fig. S1.1(a). We optimize each of the gates in U_{evol} . To optimize a target gate, we first contract all of the tensors except for the target gate and obtain a four-leg tensor G^\dagger in the left and right top panels of Fig. S1.1(b). As in the right bottom panel of Fig. S1.1(b), the SVD is executed for G , i.e., $G = USV^\dagger$, where U and V are unitary matrices, and S is a singular value matrix. Then, $G_{\text{opt}} = UV^\dagger$ is the optimal gate to maximize $\text{Re} \text{Tr}\left[U_{\text{ref}}^\dagger U_{\text{evol}}\right]$. This optimization is performed for each gate. As shown in Fig. S1.1(c), gate optimization is performed in the order of sweeping up and down the zigzag path from left to right. The initial gate was prepared by QR decomposition of the identity operator plus a small random unitary operator. The numbers of sweeps were 1,000 for the Hubbard models and 10,000 for butadiene. To reduce the number of contractions, the upper and lower portions of the target gate are stored as an environmental tensor (red) and used as needed as in Fig. S1.1(d), and the cost of contracting the tensor network is $\mathcal{O}(\chi d_{\text{evol}} 2^{4+2\lceil d_{\text{evol}}/2 \rceil} + \chi^2 2^{2+2\lceil d_{\text{evol}}/2 \rceil})$, where χ is the maximum bond dimension in U_{ref}^\dagger (22). Note that in this study, when creating the U_{ref}^\dagger

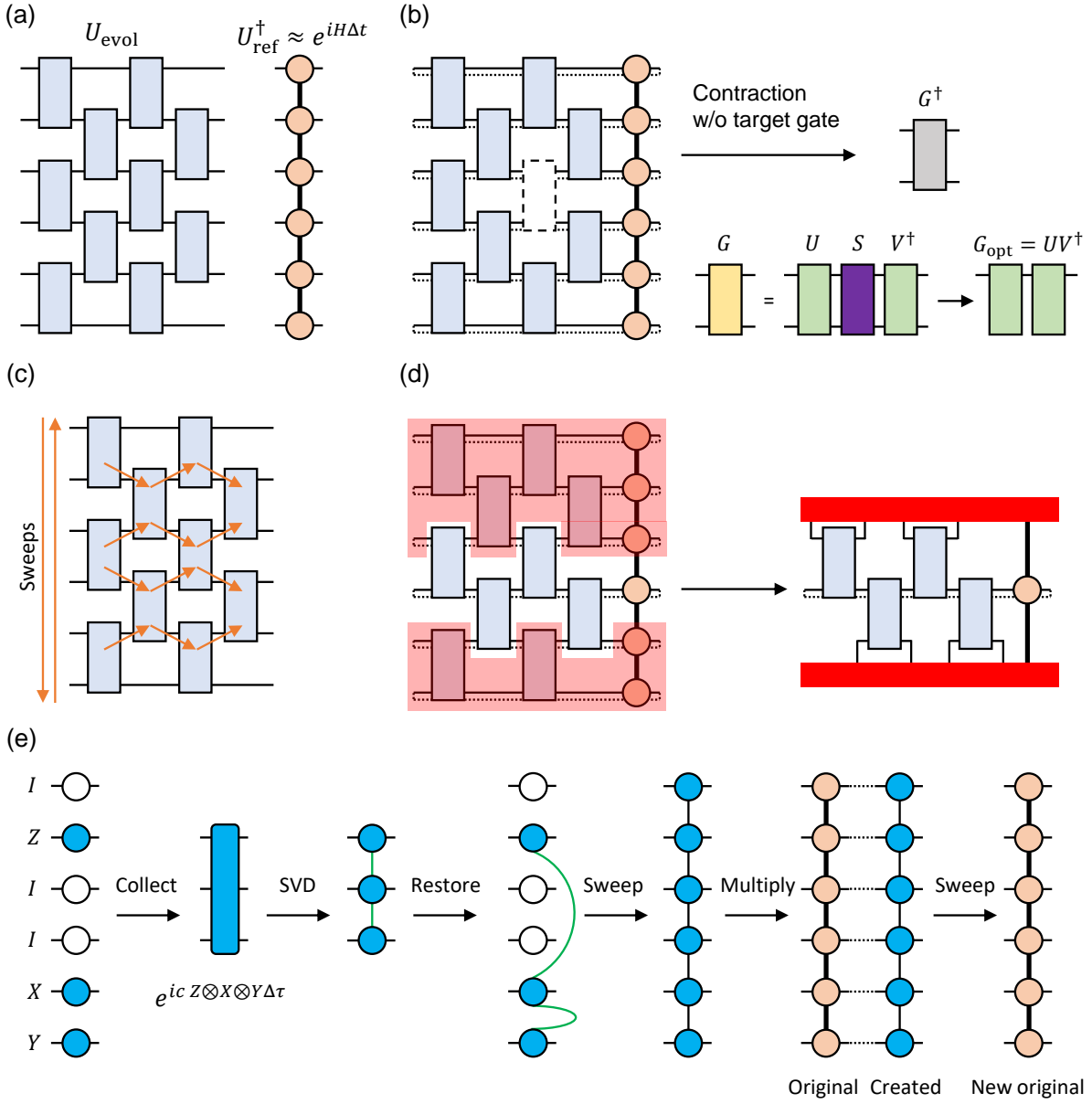


Fig. S1.1: Procedure of a unitary compression. Here is an example of six qubits and $d_{\text{evol}} = 4$. (a) Introduction of MPOs. Horizontal lines represent qubits. Vertical bold lines in U_{ref}^\dagger represent MPO virtual bonds. (b) Gate optimization. The dashed box represents a target gate to optimize. The dotted line connecting the left end and the right end represents a trace. (c) Optimization sequence. (d) Environmental tensors. (e) Example of creation of time evolution operator of $\exp\{ic(I \otimes Z \otimes I \otimes I \otimes X \otimes Y)\Delta\tau\}$.

in Fig. S1.1(a), we reduce the computational cost by calculating the time evolution operators by excluding the identity operators from the tensor product of Pauli operators in a Hamiltonian. Specifically, as in the example of Fig. S1.1(e), the following procedure is repeated for each term of the Hamiltonian; collecting only the Pauli X , Y , and Z operators, performing time evolution operations, restoring them to their initial MPO sites using SVD, converting them to MPO by sweeping, and multiplying the created MPO by the original MPO to make a new original MPO. The initial original MPO is identity, c is a coefficient in the term, and $\Delta\tau = \Delta t/200$ in our case of second-order Trotter approximation.

To execute the unitary compression of U_{prep} , we need to prepare $|\text{MPS}\rangle = \frac{1}{\sqrt{2}}(|0\rangle|\psi_g\rangle + |1\rangle|\psi_{\text{ex}}\rangle)$. We calculate $|\psi_g\rangle$ by the DMRG, and $|\psi_g\rangle$ is an MPS as

$$|\psi_g\rangle = \sum_{\vec{a}} \sum_{\vec{s}} A_{s_1 a_1} A_{s_2 a_1 a_2} \dots A_{s_N a_{N-1}} |\vec{s}\rangle, \quad (\text{S1.12})$$

where $\vec{a} = a_1 a_2 \dots a_{N-1}$, $a_\iota \in \{0, 1, \dots, \chi_\iota - 1\}$ ($\iota = 1, 2, \dots, N-1$) represents a virtual index, χ_ι is a bond dimension, $\vec{s} = s_1 s_2 \dots s_N$, and $s_\kappa \in \{0, 1\}$ ($\kappa = 1, 2, \dots, N$) represents a physical index. $|0\rangle|\psi_g\rangle$ can be represented as an MPS using a dummy tensor A_{s_0} ,

$$|0\rangle|\psi_g\rangle = \sum_{\vec{a}} \sum_{s_0, \vec{s}} A_{s_0} A_{s_1 a_1} A_{s_2 a_1 a_2} \dots A_{s_N a_{N-1}} |s_0 \vec{s}\rangle, \quad (\text{S1.13})$$

where A_{s_0} ($s_0 \in \{0, 1\}$) is a tensor of $A_0 = 1$ and $A_1 = 0$. $|0\rangle|\psi_{\text{ex}}\rangle$ can also be expressed in an MPS by the same procedure as above,

$$|1\rangle|\psi_{\text{ex}}\rangle = \sum_{\vec{a}'} \sum_{s_0, \vec{s}} A'_{s_0} A'_{s_1 a'_1} A'_{s_2 a'_1 a'_2} \dots A'_{s_N a'_{N-1}} |s_0 \vec{s}\rangle, \quad (\text{S1.14})$$

where \vec{a}' is denoted in the same way as \vec{a} previously mentioned, and A'_{s_0} is a tensor of $A'_0 = 0$ and $A'_1 = 1$. We add the two states to prepare an unnormalized superposition state,

$$|0\rangle|\psi_g\rangle + |1\rangle|\psi_{\text{ex}}\rangle = \sum_{\tilde{a}_0 \vec{a}} \sum_{s_0, \vec{s}} \tilde{A}_{s_0 \tilde{a}_0} \tilde{A}_{s_1 \tilde{a}_0 \tilde{a}_1} \tilde{A}_{s_2 \tilde{a}_1 \tilde{a}_2} \dots \tilde{A}_{s_N \tilde{a}_{N-1}} |s_0 \vec{s}\rangle, \quad (\text{S1.15})$$

where

$$\begin{aligned}\tilde{A}_{s_0\tilde{a}_0} &= \begin{cases} A_{s_0} & \text{if } \tilde{a}_0 = a_0 \\ A'_{s_0} & \text{if } \tilde{a}_0 = a'_0 \end{cases} \\ \tilde{A}_{s_1\tilde{a}_{\ell-1}\tilde{a}_\ell} &= \begin{cases} A_{s_\ell a_{\ell-1} a_\ell} & \text{if } \tilde{a}_{\ell-1} = a_{\ell-1}, \tilde{a}_\ell = a_\ell \\ A'_{s_\ell a'_{\ell-1} a'_\ell} & \text{if } \tilde{a}_{\ell-1} = a'_{\ell-1}, \tilde{a}_\ell = a'_\ell \\ 0 & \text{otherwise} \end{cases} \\ \tilde{A}_{s_N\tilde{a}_{N-1}} &= \begin{cases} A_{s_N a_{N-1}} & \text{if } \tilde{a}_{N-1} = a_{N-1} \\ A'_{s_N a'_{N-1}} & \text{if } \tilde{a}_{N-1} = a'_{N-1} \end{cases}\end{aligned}\quad (\text{S1.16})$$

$\tilde{a} \in \{\vec{a}, \vec{a}'\}$, and $\tilde{a}_0 \in \{a_0 = 0, a'_0 = 1\}$. That is, the superposition state can be represented as an MPS. $|\text{MPS}\rangle$ is obtained by normalization and transformation to the left canonical form of the superposition state.

The optimization procedure of a brick-wall MPO U_{prep} to approximate $|\text{MPS}\rangle$ is almost the same as U_{evol} since we can execute the same procedure by substituting U_{evol} to U_{prep} and U_{ref}^\dagger to $|0\rangle^{\otimes N+1} \langle \text{MPS}|$ in $\text{Re} \text{Tr} [U_{\text{ref}}^\dagger U_{\text{evol}}]$ of Eq. (S1.11), that is,

$$\text{Re} \text{Tr} [|0\rangle^{\otimes N+1} \langle \text{MPS}| U_{\text{prep}}] = \langle \text{MPS}| U_{\text{prep}} |0\rangle^{\otimes N+1}, \quad (\text{S1.17})$$

which is the same as in Eq. (2). The number of sweeps was 1,000 for all the models. Note that MPS can be embedded with sequential gates without optimization (19), but it was not adopted in our case because of the increasing depth and idle time of each qubit.

The remaining calculation conditions are described as follows. The unitary compression was implemented in ITensor (45) package of the Julia language. Hamiltonian prepared by Qiskit (see Sec. S1.3) was converted to an ITensor format, and U_{prep} and U_{evol} obtained by unitary compressions were saved in NumPy (46) format, and then the phase difference estimation was performed using Qiskit with the compressed gates. The number of the DMRG sweeps when preparing $|\text{MPS}\rangle$ was set to 20, the maximum bond dimension in SVD was set to 10 for the first 3 sweeps, 50 for the next 12 sweeps, and 1,000 for the last 5 sweeps, and the cutoff threshold in SVD was 10^{-12} for the Hubbard models and 10^{-8} for butadiene. The DMRG of the excited states was executed to reduce overlap with the MPS of the ground state.

S1.3 Model construction

Qiskit (30) was used for the fermionic model construction and Jordan–Wigner transformation for the Hubbard models and butadiene. The electronic structure of butadiene was calculated by the PySCF package (47), and the geometry was optimized using the Hartree–Fock method with the 6-31G* basis set by the PySCF and geometricTRIC (48) packages. The molecular orbitals were localized by Boys localization (35) for π and π^* orbitals, and a fermionic Hamiltonian was constructed as an eight-qubit CASCI (4e 4o) problem.

The orbital order was optimized using a genetic algorithm implemented with the DEAP library (49). The cost function is C in Eq. (4), the parameters were set with a population size of 50, a crossover probability of 70%, a mutation probability of 20%, and 100 generations. Ordered crossover and index-shuffling mutation were applied, and tournament selection with a size of three was used. Note that while we utilized the Jordan–Wigner transformation after the reordering, incorporating fermion-qubit mappings considering circuit topology (50, 51) are left for future work.

S2 Supplementary Text

S2.1 Error analysis for the algorithm

We note the error robustness in our algorithm. Assume the global depolarization channel for the state before the measurement $|\phi\rangle$ in Eq. (S1.7),

$$\mathcal{E}(|\phi\rangle\langle\phi|) = (1 - p_{\text{dep}})|\phi\rangle\langle\phi| + p_{\text{dep}}\frac{1}{2^{N+1}}I^{\otimes N+1}, \quad (\text{S2.1})$$

where p_{dep} is an error rate of the depolarization channel. The probability in Eq. (S1.8) becomes

$$\text{Tr}\left[|0\rangle\langle 0|^{\otimes N+1}\mathcal{E}(|\phi\rangle\langle\phi|)\right] \approx (1 - p_{\text{dep}})\frac{1}{2}(1 + \cos(E_{\text{gap}} - \varepsilon)t) + \frac{p_{\text{dep}}}{2^{N+1}}, \quad (\text{S2.2})$$

and the error does not change the peak position while the amplitude decreases. In addition, the second term, which comes from the effect of depolarization noise, is exponentially decaying with respect to N . When calculated with a similar setup in QPE [Fig. 1(a)] and QPDE [Fig. 1(b)], the second term becomes $p_{\text{dep}}/2$, i.e., constant, due to the ancilla-only measurement (13). Therefore, the exponentially small noise affection is a feature of our algorithm.

The affection of the decay actually can be seen in the results of the real device execution. For example, for the eight-qubit Hubbard model, the value of the second term of noise is $\frac{1}{2^9} \approx 0.0020$ at maximum. In fact, a uniform distribution of magnitude can be seen in the latter half of the iterations in Fig. 3(b) and Figs. 5(c) and (d). On the other hand, the value in 21-qubit is $\frac{1}{2^{21}} \approx 4.8 \times 10^{-7}$, and thus the sharp peak can be seen of Figs. 3(c) despite a small signal of 0.01 magnitude. As related data, the 20 qubit Hubbard model without error suppression is shown in Fig. S2.1. A small peak is seen at the beginning, but the signal disappears with the proceeding iteration. In the final iteration, there is no signal at all, meaning that there is not only no signal but also no noise effect. These results suggest that our algorithm can estimate the energy for large qubits as long as the signal is detected.

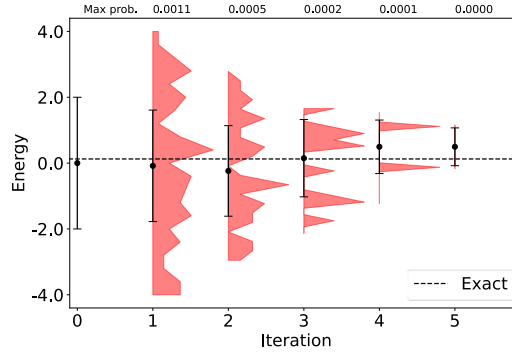


Fig. S2.1: Demonstration of our algorithm in the one-dimensional Hubbard models using the Heron device *ibm_torino* without the error suppression (21-qubit circuit). The circle and error bar denote the mean value and standard deviation, respectively, of the posterior distribution in the iteration. The sampled probabilities are shown in red, and each plot is normalized by the maximum value in each iteration, which is shown at the top of the plot.

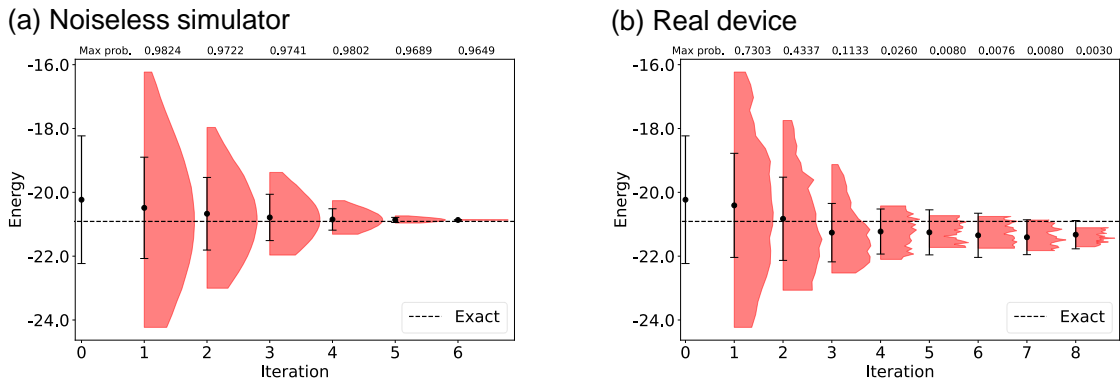


Fig. S2.2: Demonstration of our algorithm for the FCI calculation in the Hubbard model (nine-qubit circuit) using (a) the noiseless simulator and (b) the Heron device *ibm_torino* with the error suppression. For ease of understanding, the signs of energy value are reversed. The circle and error bar denote the mean value and standard deviation, respectively, of the posterior distribution in the iteration. The sampled probabilities are shown in red, and each plot is normalized by the maximum value in each iteration, which is shown at the top of the plot.

S2.2 FCI energy calculation

The FCI energy can be calculated by substituting $|\psi_{\text{ex}}\rangle$ for a vacuum state $|0\rangle^{\otimes N}$ in the superposition state. Since the vacuum state is trivially MPS and the energy of the vacuum state is zero, Eq. (S1.8) becomes

$$\text{Tr}\left[|0\rangle\langle 0|^{\otimes N+1}|\phi\rangle\langle\phi|\right] \approx \frac{1}{2}(1 + \cos(E_g + \varepsilon)t), \quad (\text{S2.3})$$

the (sign reversed) ground state energy can be calculated in our algorithm. Fig. S2.2 shows the demonstration of the eight-qubit Hubbard model, where U_{evol} was shared with the gap estimation in the main text, U_{prep} was prepared by $d_{\text{prep}} = 6$ with $f(U_{\text{prep}}; |\text{MPS}\rangle) = 0.99$, and μ_{init} was set to the value when the DMRG is performed with the maximum bond dimension as two. The results of the noiseless simulator in Fig. S2.2(a) show that the distribution approaches the exact solution with each iteration. The final value is -20.866 ± 0.005 , where the exact solution is -20.911 . We also confirmed that the algorithm works on the real device (especially when the maximum probability in an iteration is greater than 0.01) in Fig. S2.2(b), where the energy of a final iteration is -21.326 ± 0.444 .